
Effects of size polydispersity on segregation of spherical particles in rotating drum

Vo Thanh-Trung ^{1,*}, Vu Thi Lo ^{2,3}, Mutabaruka Patrick ⁴

¹ Bridge and Road Department, Danang Architecture University, Da Nang city, Vietnam

² Division of Computational Mathematics and Engineering, Institute for Computational Science, Ton Duc Thang University, Ho Chi Minh City, Vietnam

³ Faculty of Civil Engineering, Ton Duc Thang University, Ho Chi Minh City, Vietnam

⁴ IFREMER, DYNECO/DHYSED, 29280, Plouzané, France

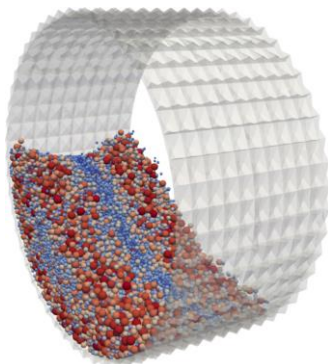
* Corresponding author : Thanh-Trung Vo, email address : trungvt@dau.edu.vn ;

vuthilo@tdtu.edu.vn ; Patrick.Mutabaruka@ifremer.fr

Abstract :

To get insight into the segregation process of a polydisperse granular materials flow, we numerically investigated the migration process of particles in a rotating drum operating in the rolling regime by means of the discrete element method. Particle migration is analyzed through the variation of the proportion of particles in different zones where the flow property is characterized. The proportion of particles in different zones of the drum shows to increase in the center of the flow radially and axially where a higher concentration of small particles is observed, while its decreases in other zones with a higher concentration of larger particles. Interestingly, we find that the migration process of particles leads to radial and axial segregation which is caused by a combination between the exerted fluctuation forces on particles and its surrounding pressure gradient.

Graphical abstract



1 Introduction

The segregation process has been a subject of particular interest in granular materials for mainly separating material. The segregation is observed for materials having higher disparity in their properties such as size polydispersity or density when materials are flowing in a particular regime [1–12]. The segregation process is used in food, mining, pharmaceutical, or iron-ore making industry [13–16]; we also observe this process in nature for phenomena such as debris flow or landslides [17–19]. The main observed segregation is based on material size disparity. A direct consequence of this size disparity is a sorting-like process based on particle size while materials are flowing forming patterns of small and large particles and thereby affecting the system evolution in terms of materials space distribution. Depending on the configuration used (free flow on an inclined plane, silo discharge or rotating drum) and the imposed flow and boundaries condition (flow rate or confining conditions), the observed segregation might be modified [20–25]. On an inclined plane or in a shear flow for example, the segregation occurs following the parallel axis of the flow with patterns of layers of particles with nearly the same size [17, 26–35] with large particles moving toward the free surface while smaller are migrating to the bottom. In the case of silo like discharge flow, large particles shows to migrate toward the center on the silos

axis where the flow velocity shows to be higher while smaller particles migrate aside [25, 36, 37]. For a rotating drum, two types of patterns are observed: 1) axial where patterns occur along the rotational axis of the drum and 2) radial with patterns appearing along the radial axis of the drum [20, 22, 38, 39] where in both cases, smaller particles migrate toward the center of the flow (axially and radially) while large particles are migrating to the extrema of the drum (side walls and to the free surface).

Despite that, all previous works provide much information from numerically and experimentally studies on the physics behind the segregation processes, they are mainly focusing on bi-disparity properties while in nature and industrial process, particles have complex shapes and the third dimension (fully three dimensions) shows that the segregation is more complex as a process; this is the case for rotating drum for example where the material flow is not in a trivial way [17, 19]. The main complexity in experimental and continuum modeling works [25, 27, 40, 41] is having access to micro-structure at the contact level that might explain the phenomena that govern the segregation while for numerical modeling using Discrete Element approach, the limitation occurs in the time-consuming that took the simulations.

In this study, we are interested in the segregation that occurs in a rotating drum for polydisperse materials by means of

numerical modeling approach using Discrete Element Method. The main concern in this paper is the representativity of a granular polydisperse material besides the possibly time-consuming. The flow in a rotating drum has several regimes [42–47]; we focus here on the rolling regime where the material flow as fluid-like. The polydisperse representative sample is generally generated using Particles Size Distribution *PSD* [10,27,48–51] that consists of generating samples composed by several classes of particles where in each class, belonging particles have the same or nearly the same diameter. At a higher size ratio in diameters, the number of particles in a constant volume increases, and this increase is proportional to the simulation time. In this paper, we used a reasonable size ratio to guarantee a reasonable simulation time. We analyze the effects of the size ratio on the flow characteristics through the migration process of particles and the possible physical origins of two distinct segregation axial and radial through the local environment surrounding particles.

In this paper, we briefly introduce the numerical method in section 2; we, in a second time, give a brief description on how samples are generated with a short description on the choice of the used parameters in section 3. In section 4, we discuss the dynamic behaviors of the flow. We analyze the segregation mechanisms in section 5 and in section 6, we conclude and gives a summary of salient results and routes of further researches.

2 Discrete Element Method

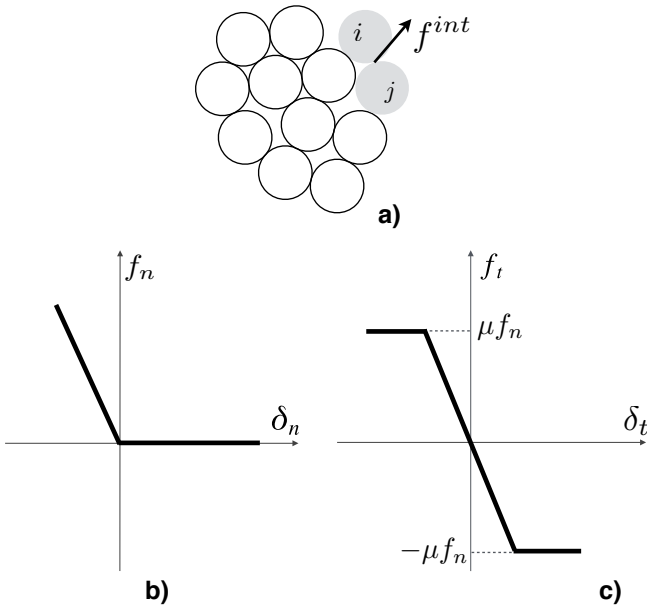


Fig. 1. (a) Geometrical contact representation between particle *i* and *j* in a collection of particles. (b) Signorini condition for the contact normal force f_n as a function of the deflection δ_n and (c) Coulomb frictional condition for the tangential force f_t as a function of the tangential displacement δ_t with threshold μf_n where μ is the frictional coefficient.

The Discrete Element Method (DEM) has been used now for several years in many applications to model granular materials [52–56]. By taking into account the particle interactions (see figure 1.(a)) and based on a step-wise integration of the equations of motion, we compute the dynamics of each particle *i* [56–60] following:

$$\begin{aligned} m_i \frac{d^2 \mathbf{s}_i}{dt^2} &= \sum_{all} \mathbf{f}_i^{int} + m_i \mathbf{g}, \\ \mathbf{I}_i \frac{d^2 \boldsymbol{\omega}_i}{dt^2} &= \sum_{all} \mathbf{M}_i^{int} \end{aligned} \quad (1)$$

where m_i , \mathbf{s}_i and \mathbf{g} are respectively the mass, position, and gravity acceleration vector of particle *i*. \mathbf{f}_i^{int} denotes the inter-particles force, \mathbf{M}_i^{int} is the moment, \mathbf{I}_i is the rotational inertia matrix and $\boldsymbol{\omega}_i$ is the rotation vector position for particle *i*.

The inter-particles forces are obtained using a frictional contact type based on a visco-elastic model within the Signorini and Coulomb friction condition (see figure 1.(b–c)). For this approach and in a more general way in contact mechanics, the contact force \mathbf{f}_i^{int} has two parts: 1) normal contact force f_n and 2) tangential contact force f_t . The normal force in DEM has to obey the Signorini condition [58]. This means that as long as there is non geometrical contact between two particles, *i* and *j*, given by the deflexion $\delta_n = |s_i - s_j| - R_i - R_j < 0$ non inter-particles contact force is calculated and if the contact exist, this one is always positive to guarantee a repulsion/separation condition. R_i and R_j are the radius of particle *i* and particle *j*. s_i and s_j are the position of particle *i* and *j*, respectively. This leads to:

$$f_n = \begin{cases} k_n \delta_n + \gamma_n \dot{\delta}_n & \text{if } \delta_n < 0 \\ 0 & \text{otherwise} \end{cases} \quad (2)$$

where k_n and γ_n are the elastic stiffness and the viscous damping, respectively. According to the the Coulomb friction law, a threshold regarding the normal force μf_n is used where, μ is the frictional inter-particles coefficient (see Fig.1.(c)) [61–64] and it's gives:

$$f_t = -\min \left\{ (k_t \delta_t + \gamma_t \dot{\delta}_t), \mu f_n \right\}. \quad (3)$$

where k_t and γ_t are tangential elastic stiffness and the corresponding viscous damping, respectively. δ_t is the cumulative tangential displacement calculated as $\delta_t = \int \dot{\delta}_t dt$ where $\dot{\delta}_t$ is the relative tangential velocity. One should notice here that $\delta_t = 0$ the first time the contact is formed, then is set to $\delta_t = -\mu \frac{f_n}{k_t} \frac{|\dot{\delta}_t|}{\dot{\delta}_t}$ when $|f_t| > |\mu f_n|$ and it is zero when the contact break.

3 Model sample settings

The particles was generated using a now well known Particle Size Distribution (*PSD*) [10,27,48,49,51,65] where a uniform distribution in term of particles volume by class was imposed. This approach guarantee a correct representative number of particles for each class and allow to recover the classic grading curve. We generated four samples composed by spherical

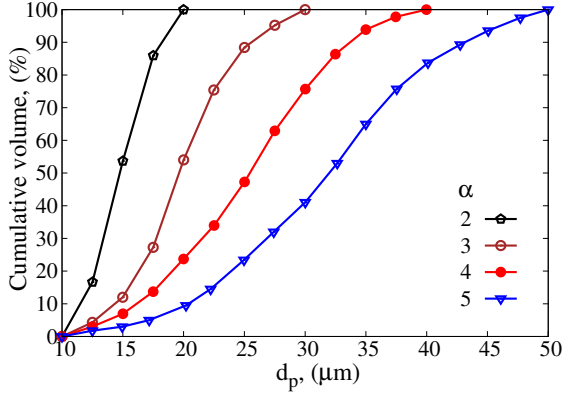


Fig. 2. Cumulative particle volume fraction as a function of the particle diameter d_p for different values of size ratio α .

particles for different size ratio $\alpha = d_{max}/d_{min}$ with d_{max} , d_{min} being the maximum and minimum particles diameter respectively. The used value of d_{min} and the covered range of α in this study are presented in Tab.1. The PSD used in this paper is based on the assumption that in each class i , the total volume is proportional to the corresponding particles volume $\sim d_i^3$ and this impose $n_i d_i^3$ to be constant where n_i is the number of particles in the considered class. For the class i , the numerical fraction of particles is P_i and has to satisfy the following constraint $\sum_i P_i = 1$; and the distribution P of particles of diameter d is given by:

$$P(d) = 2 \frac{d_{max}^2 d_{min}^2}{d_{max}^2 - d_{min}^2} d^{-3} \quad (4)$$

The grading curve of our generated samples are shown on Fig.2 where for each sample, we fixed the maximum number of generated particles to 50000.

The sample preparation follow two steps: 1) in the first step, once particles size is generated, they are placed on a Cartesian grid inside the drum with the filling degree of 20%, maintaining the PSD conditions and the total number of particles at 50000, this then imposes the drum diameter for each value of α , 2) in a second step, the gravity is activated and a short simulation is performed until the settling procedure is finished. The final state after the settling procedure is shown in figure 3.(a) for $\alpha = 5$. While particles are spheres and free, the drum is composed of an assembly of tetrahedral particles (see Fig. 3) with two lateral walls not represented here; the degree of freedom of all tetrahedral particles are then controlled to finally impose the drum rotation.

The flow in a rotating drum can be characterized by the Froude number Fr but also the percentage of the filling degree of material in the drum. The Froude number represent the ratio between the kinetic energy and the gravitational potential energy of particles composing the flowing material. For a rotating drum this leads to $Fr \propto \Omega^2 d_c / g$ [44, 42, 66]. Ω is the drum rotational speed, d_c is the drum diameter and g is the gravitational acceleration. The filling degree represent the proportion of the drum volume occupied by the filled materials. As the flow has to be consistant and continuous, we fixed $Fr = 0.25$ and the drum was filled up to 20% for each value of α .

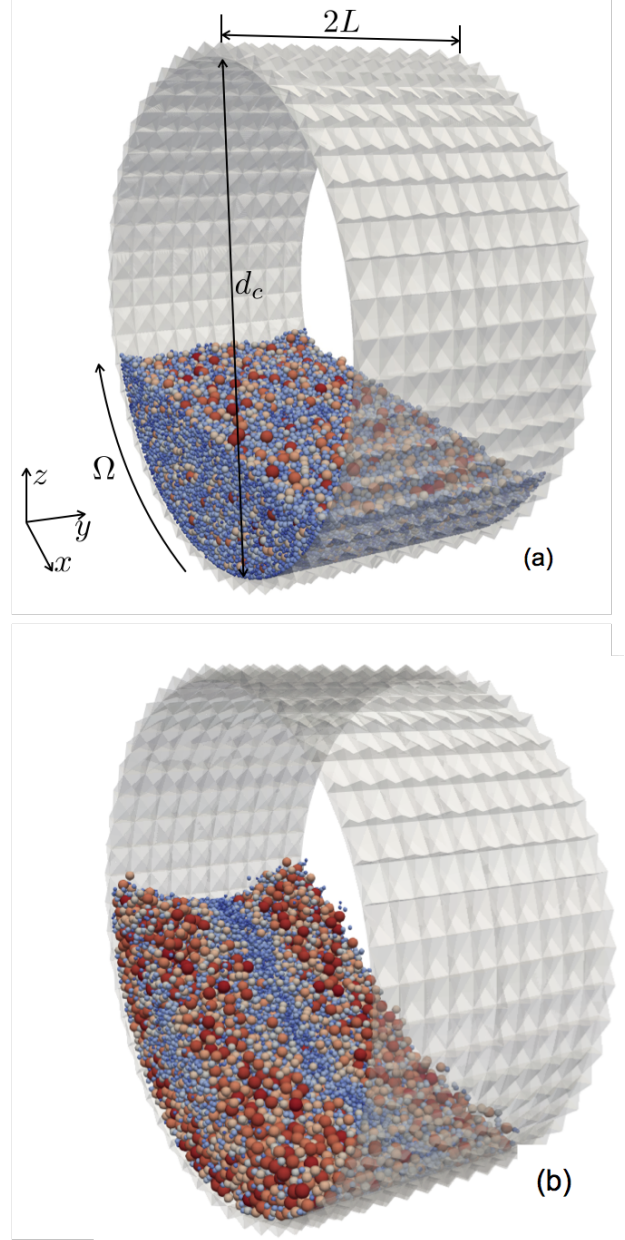


Fig. 3. Particles distribution after the settling step in the drum at $N_r = 0$ with the drum size (axial length $2L$ and the diameter d_c) and imposed angular rotation velocity Ω (a). Final particles distribution at $N_r = 20$ in the drum (b). Both figures are made for the size ratio $\alpha = 5$, the color map indicates the particle size.

The choice of the used physical parameters such as the particles density or the size distribution as well as the filling level is based on the granulation process of iron-ore in a rotating drum [50, 67]. Classically in DEM to guarantee a lower elastic deflection, the particle stiffness is chosen based on the ratio between the elastic deflection (at its contact point under the loading correspond to the weight of the particle) and the d_{min} and, this has to be at least below 0.01. This ensures the particle to be considered nearly as a rigid body with a negligible contact deformation. Due to numerical constraints, the particles stiffness was fixed at a reasonable value as it imposes the

Table 1. Parameters used in these simulations

Parameter	Symbol	Value and Unit
Minimum particle diameter	d_{min}	10 μm
Size ratios	α	[2,5]
No. of particles	N_p	50,000
Filling level	f	20 %
Drum diameter	d_c	[1480,1800] μm
Friction coefficient	μ	0.5
Normal stiffness	k_n	100 N/m
Tangential stiffness	k_t	80 N/m
Normal damping	γ_n	$5 \cdot 10^{-5}$ Ns/m
Tangential damping	γ_t	$5 \cdot 10^{-5}$ Ns/m
Particles density	ρ	3500 $\text{kg} \cdot \text{m}^{-3}$
Time step	δt	10^{-7} sec

compressibility of the material and therefore the time stepping. In our work, the tangential stiffness k_t of particles is 80% of the value of the normal stiffness k_n . Under their own weight, two particles in contact with one of them fixed, the static maximal force is given by $f_n = mg = k_n \delta_n$; with $\langle \delta_n \rangle = a d_{min}$ and $m = \pi \rho d_{min}^3 / 6$, this leads to $a = (1/6) \pi d_{min}^2 \rho g / k_n$. Based on our parameters (see Tab.1), $a \simeq 2 \times 10^{-8}$ which is small enough for our assumptions of rigid-like particles ($\langle \delta_n \rangle / d_{min} \ll 0.01$). The rest of the parameters used in this paper are summarized in Tab.1.

4 Flow characterization

The particles flow in the rolling regime has a fluid-like flow with two main distinct regions: 1) an downward region known as the *passive region* where particles are sheared and accelerated by the drum wall toward the drum rotation until particles reach a dynamic slope angle of $\beta \sim 40.75 \pm 1.75$ degree from the vertical z -axis as we observe on Fig.4 and, 2) the upward region known as the *active region* where particles flow in the opposite direction and are sheared and controlled by gravitational acceleration. Once particles reached the drum wall at the downstream, they enter again in the passive region as we observed in Fig.4. In between these two regions, the limit is characterized by particles with a velocity field that is nearly zero as we observe in Fig.4. We should notice here that β should vary with Ω and the total mass of particles wherein our simulations the total mass is controlled by the filling degree. In fact, when Ω increases, β decreases due to the increase of the centrifugal force; on the other hand, increasing the particle mass, introduces the inertia effect in the centrifugal force that decreases also the value of β . Besides the radial ($X-Z$ plan) flow characterization, we also analyzed the axial flow on Y -axis. Figure 5 shows the velocity field with a color map giving the axial velocity magnitude v_y . We see on this figure that there is a non-negligible effect of the lateral walls that it is imposing a flow of the particles from the lateral walls toward the center of the drum when they leave the passive region to (upstream) the active region while they are pushed again to the lateral wall when they migrate from the active to the passive region at the downstream.

In contrast with figures 4 and 5, we tracked the trajectories of smaller and larger particles from four different positions.

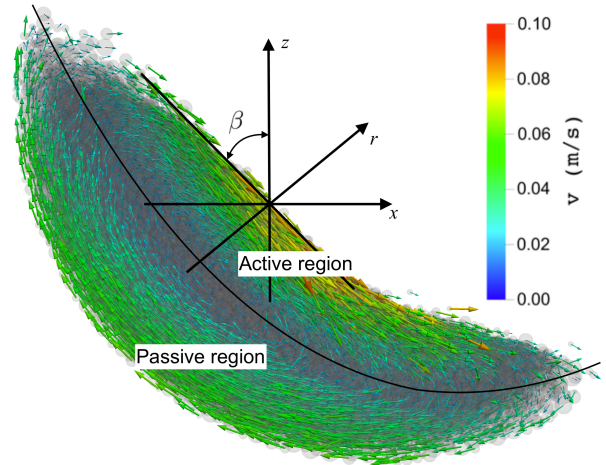


Fig. 4. The active-passive regions of a granular flow in a rotating drum for the sample of the size ratio $\alpha = 5$ (A snapshot of the flow after 20 cycles in $X-Z$ plan view). The color map on field represents the particles velocity magnitude. β is the dynamic slope angle from Z axis and r is the radial axis defined to be always perpendicular to the free surface of the flow.

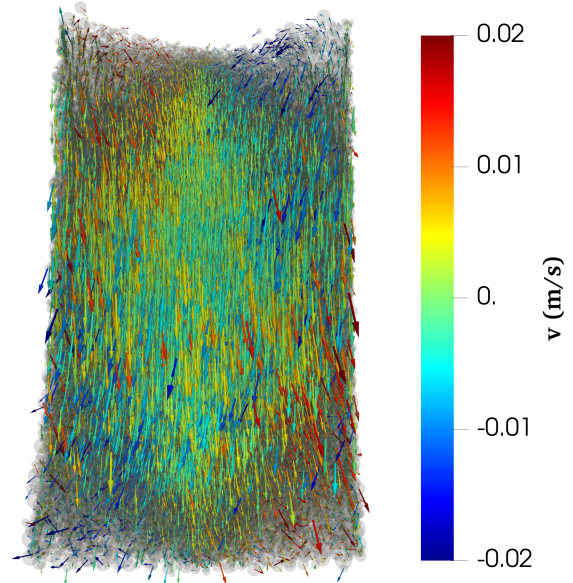


Fig. 5. A snapshot of the flow after 20 cycles. Velocity field for $\alpha = 5$ in $Y-Z$ plan view. The color map on the field indicate the velocity magnitude along Y axis.

Figure 6 shows the trajectory for radial and axial view of a smaller and larger particle from their initially position at the beginning of the simulation for the first drum rotational cycle $N_r = 0$ (green on the color map) up to $N_r = 20$ (red on the color map). Figure 6(a) shows the radial trajectory of a small particle going from the extrema toward the center while Fig. 6(d) shows the radial trajectory of a large particle that is migrating from the center to the extrema as N_r increases. In the same way, we tracked the trajectory of a small particle Fig. 6(b-c) (in a $Z-Y$ and $X-Y$ plan view, respectively) for axial migra-

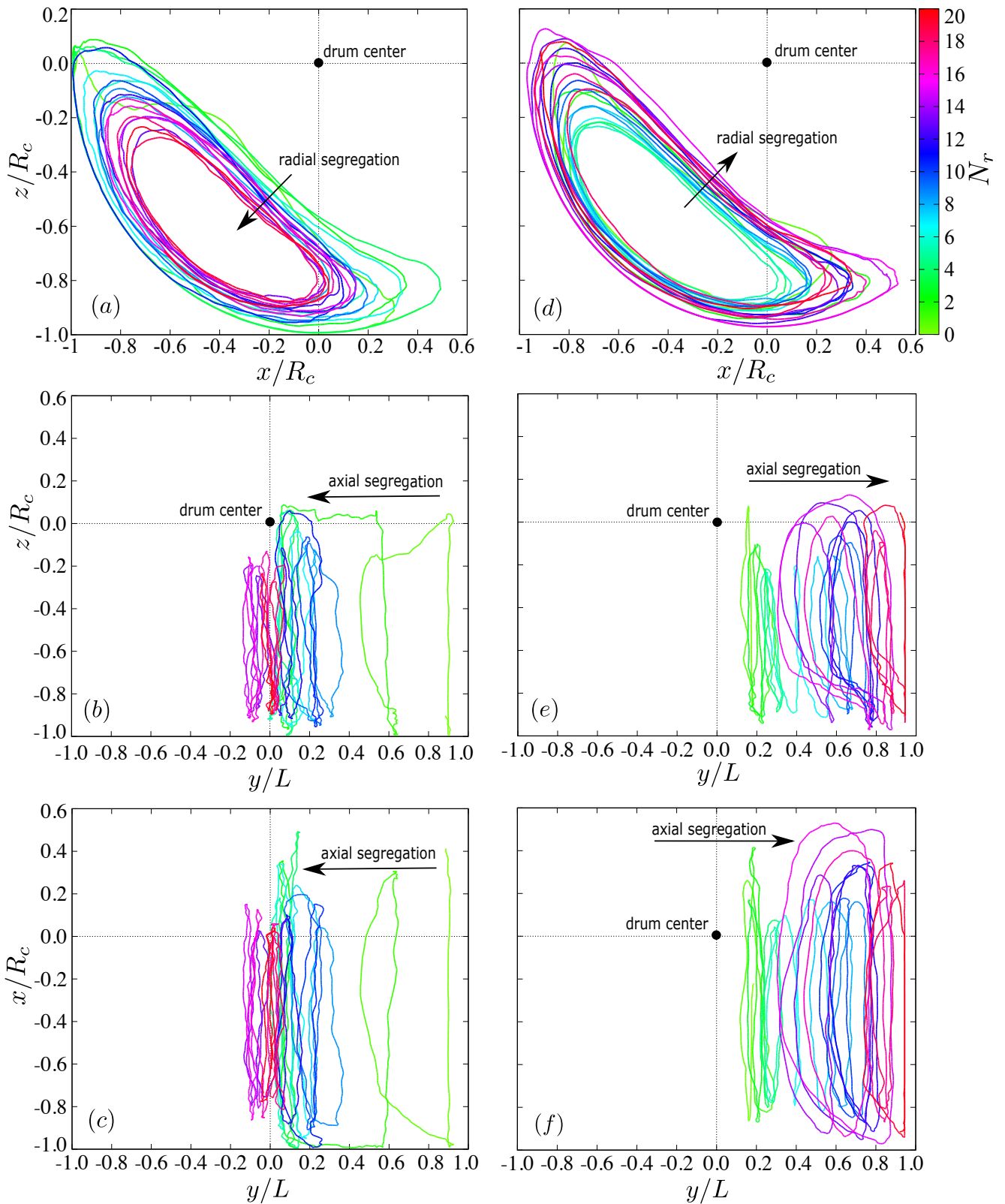


Fig. 6. A six ways representation characterizing the particles trajectory during the flow. Radial small (a) and large (d) particles trajectory; an $X-Z$ plan view. Axial small (b-c) particles trajectory for the $Z-Y$ respectively $X-Y$ plan view. Axial large (e-f) particles trajectory for the $Z-Y$ respectively $X-Y$ plan view. The color map represent the number of rotation N_r of the drum starting from zero (initial configuration) to 20 (final configuration).

tion; we observe in these two plans views that the small particle migrate from the lateral extrema position (at the the $y = L$) to the center of the drum (at $y = 0$) while the inverse migration is observed for large particle on Fig. 6(e–f). Figures 6(a–f) gives a more visually way of this migration but still can not explain the mechanisms that are at the origine of such segregation; we, in section 5, will discuss more on this in detail.

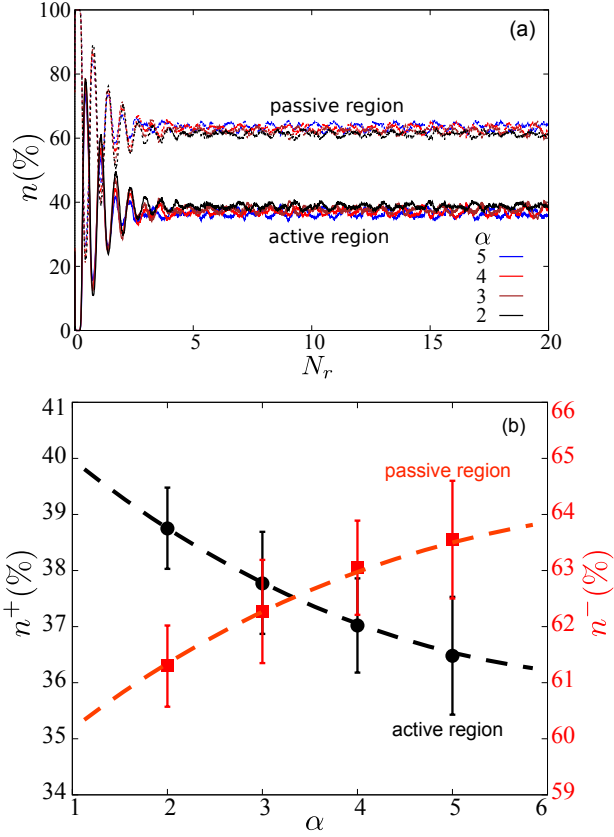


Fig. 7. (a) Percentage number n of particles in the active and passive regions as a function of the number of rotations of drum for different values of α . (b) Average of percentage number of particles in the active n^+ (●) and passive n^- (■) regions from $N_r = 5$ to $N_r = 20$ for different value of α . The dashed lines represent the fits.

In a more qualitative way, to characterize this migration, we measured the evolution of the proportion of particles in a selected zones during the rotation of the drum corresponding to the actual number of particles in the selected zone over the total number of particles in the drum. Figure 7.(a) shows the proportion n of particles in the active and passive regions as a function of the number of rotations of the drum for different values of α . We observe that after five rotations, the proportion n for the passive region is stabilized at $\sim 62.5\%$ and $\sim 37.5\%$ for the active region. This means that for a given filling degree and Ω , once the flow is established the two regions are explicitly defined. Looking closely, after the five first rotations, we observe a small influence of the size ration α . Calculating the average of this proportion number of particles in the active region n^+ and the passive region n^- between 5 and 20 rotations, we found that the proportion n^- of the passive region increasing with α

and shows to be tending to a plateau at a higher value of α (see Fig. 7(b)). This implies a decreasing proportion number of particles n^+ in the active region that shows also to be tending to a plateau (see Fig. 7(b)); this was also observed by Yang et al [10]. In the same way, we analyzed the migration of particles through the evolution of the proportion of particles in the passive-active region, we evaluated the evolution of the axial proportion of particles n^a in three different zones A, B and C (see Fig. 8 the position of each zone) and the radial proportion of particles n^r in zone D (see Fig. 8 the position of zone D). Figure 9 shows the evolution of n^a for different values of α in zone A, B and C where in all zones n^a start at $\sim 20\%$; we, at first, found that while in zone A and B n^a increases with N_r and be tending to a plateau at higher values of N_r , in zone C, n^a is decreasing and it's also tending to plateau at higher values of N_r . It was also found that while in zone A and B increasing α is increasing n^a , the inverse tendency is observed in zone C. Figure 10 shows the evolution of the radial proportion n^r for different values of α in zone D. We observe here that n^r increases from 52% rapidly before it tend a plateau at higher values of N_r . The radial particle proportion n^r also increases with α .

The evolution of the particles proportion n^+ , n^- , n^a and n^r indicate a clear migration of particles from one zone to another. In fact, for the same occupied volume, when there is a higher number of large particles than small particles, the proportion of the particles will be less and vice versa. As for all our initial samples, the particle space distribution is homogeneous, the evolution of n^+ , n^- , n^a , and n^r indicate a size-based migration. From Fig.9 and Fig. 10, the variation of this proportion indicates that small particles migrate for the drum extreme toward the center (to zone A) respectively to zone D while it's decreasing in zone C respectively out on zone D. Therefore, preferential migration based on particle size is a first indicator of the segregation behavior of polydisperse materials while is flowing inside a rotating drum. We will discuss more in detail this particle's segregation process and its physical origins in section Sec. 5.

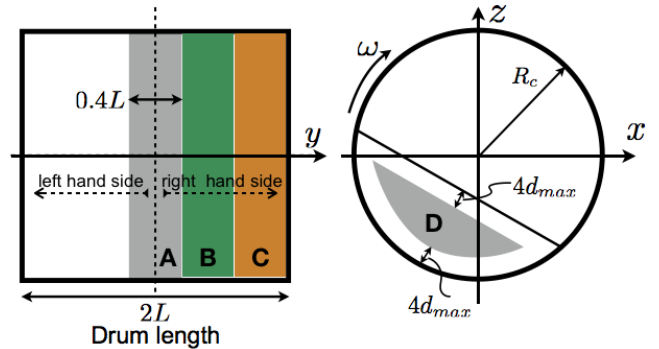


Fig. 8. (left figure) Schematic representation of three axial zones along the drum length and delimitation of the left and right hand side of the drum based on Y axis symmetry. (right figure) A schematic representation of the zone D where radial particles migration are calculated.

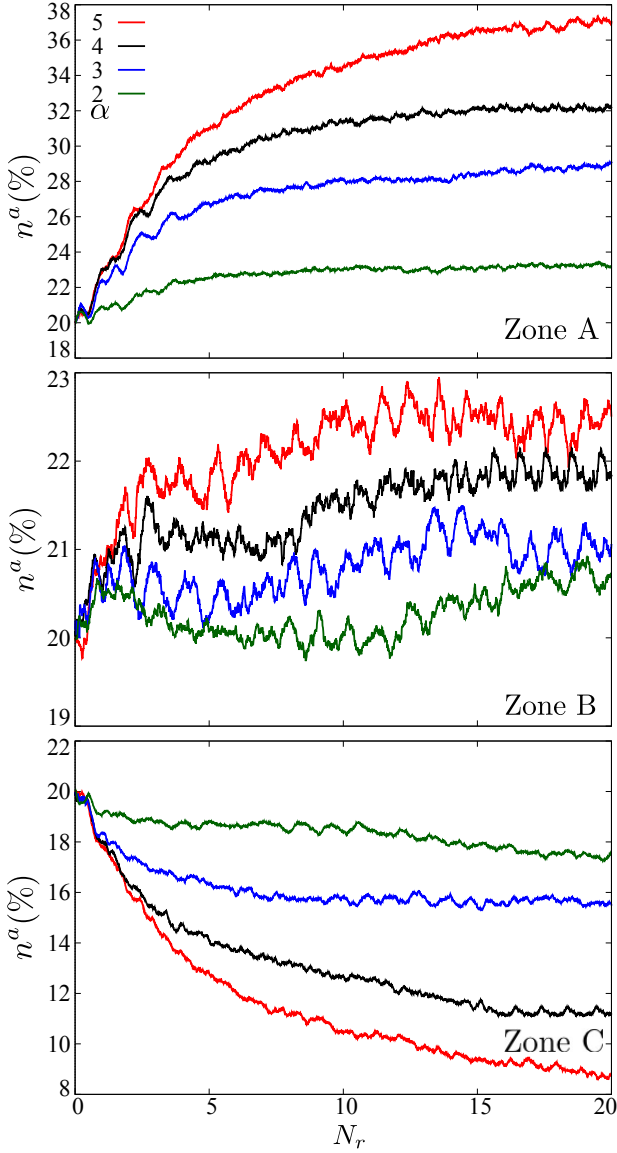


Fig. 9. Evolution of n^a as a function of N_r for different value of α in zone A, B and C (see Fig. 8).

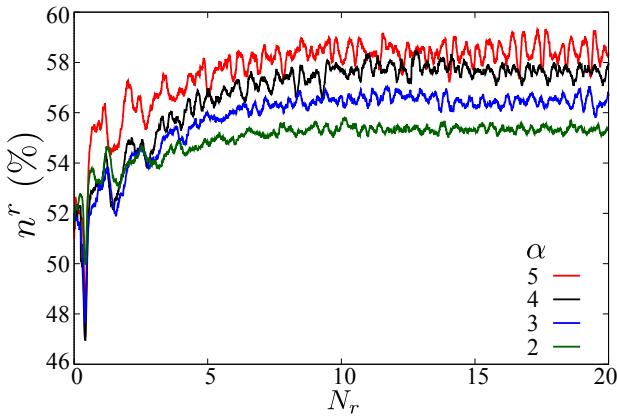


Fig. 10. Evolution of n^r as a function of N_r for different value of α in zone D (see Fig. 8).

5 Segregation mechanisms process

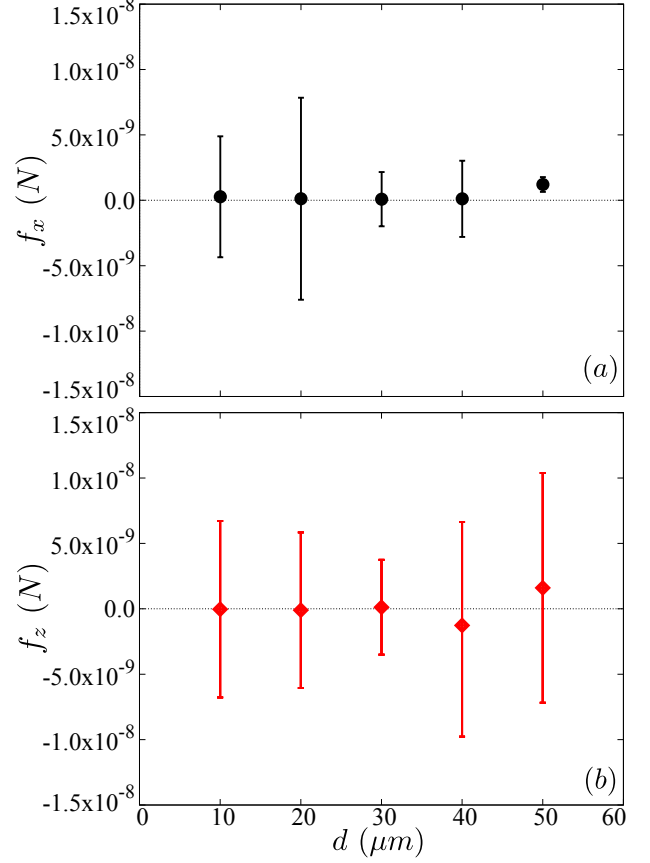


Fig. 11. Exerted time-averaged force (on 20 rotational cycles) on particles as a function of particle diameter for $\alpha = 5$. (a) Projected force on X axis and (b) projected force on Z axis.

The segregation process in polydisperse granular materials flowing shows to be governed by a surrounding particle pressure effect and the exerted force on particles during the flow [26, 31, 34, 35]. In the case of a gravity driven flow, there exists a natural pressure gradient that leads to migration behaviour of large particles during the flow toward the lower pressure [30, 31]. One might expect a direct measurement of a lift force on these large particles that should indicate the migration direction, however, this can occur even when there is non trend in the force applied on these large particles but this force plays more a role in his fluctuation [26]. As discussed from Sec. 4, two types of segregation based on particles migration are observed: 1) radial segregation and 2) axial segregation.

Figure 11 shows the the time average force (on 20 rotational cycles) on X-axis (Fig. 11.(a)) and on Z-axis (Fig. 11.(b)), both forces expressed for five selected diameters for the case of $\alpha = 5$. The two forces gives the radial for as $f_r = f_x \cos(\theta) + f_z \sin(\theta)$. As observed by [26], there is non clear trend, however, we observe an important fluctuation in their error bar. In additional to this radial force variation, we investigated the radial pressure σ_{rr} ; with $\sigma_{rr} = A^T \sigma A$, A is a transformation matrix and

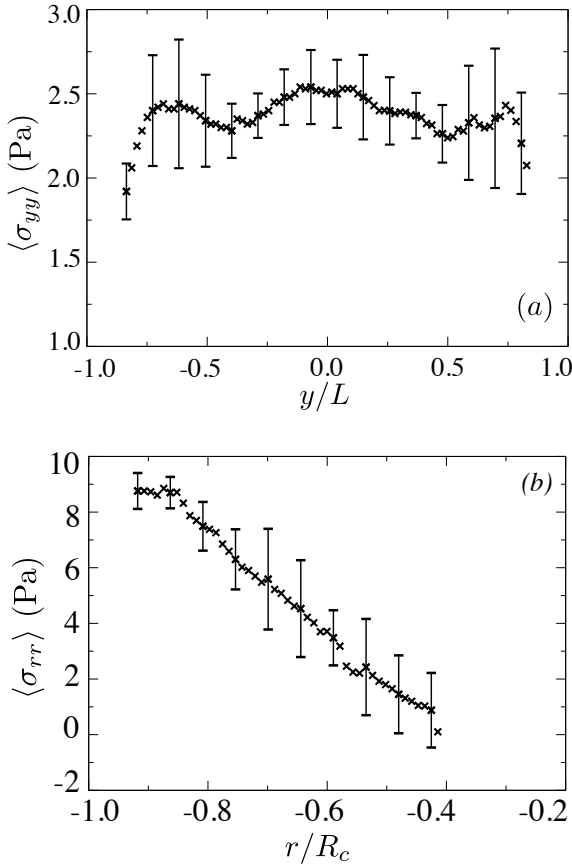


Fig. 12. (a) Axial time-averaged confining stress $\langle \sigma_{yy} \rangle$ as a function of the normalized drum axial position y/L . (b) Radial time-averaged confining stress $\langle \sigma_{rr} \rangle$ as a function of the normalized drum radial position r/R_c . Both figures computed for $\alpha = 5$.

σ is the stress tensor in cartesian coordinates defined as

$$A = \begin{bmatrix} \sin\beta & 0 & \cos\beta \\ 0 & 1 & 0 \\ -\cos\beta & 0 & \sin\beta \end{bmatrix}$$

$$\sigma = \frac{1}{V} \sum_{c \in V} l^c \otimes f^c$$

where V is the selected volume, l^c is the branch vector connecting the center of mass of two particles in contact, f^c is the contact force and \otimes denotes the dyadic product and the summation runs over all contacts in the selected volume. Figure 12(b) shows the profile of σ_{rr} pressure as a function of the radial position r normalized by the drum radius R_c . One should expect large particles to only at the free surface of the flow, but due the particular flow characteristic these particles once reach the downstream they reenter in the passive regime where with the contribution of the the centrifugal force they stay near the drum wall. The flow characteristic imply a radial segregation of large particles at the extrema while smaller migrate to the center on the flow (in zone D).

The axial segregation as well as for the radial segregation is due to the pressure gradient and the fluctuation in the force ex-

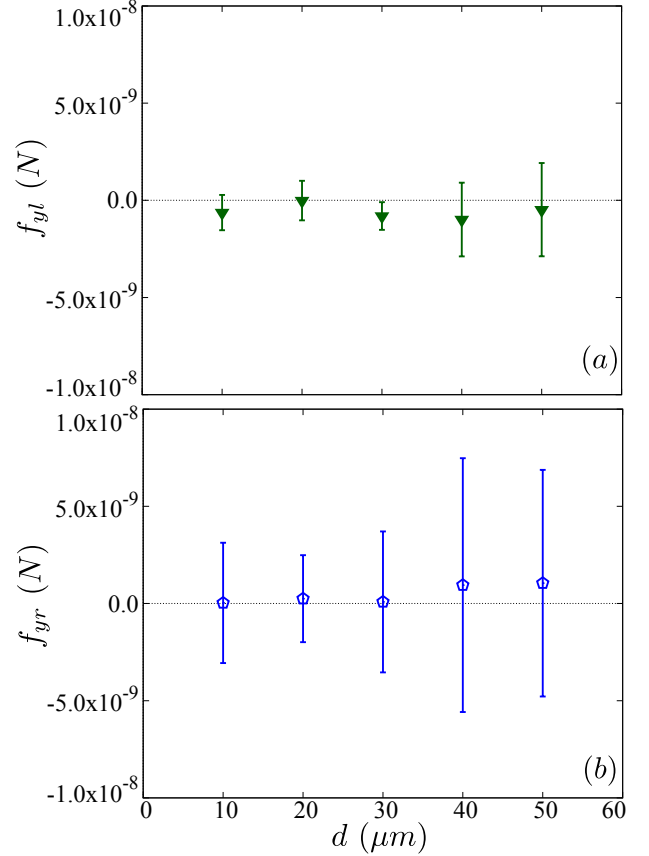


Fig. 13. Exerted time-averaged force on particles as a function of particle diameter for $\alpha = 5$. (a) projected force on Y -axis for the left hand of the drum and (b) projected force on Y -axis for the right hand of the drum.

erted on particles along the Y -axis. The pressure gradient here is a direct consequence of the presence of the lateral wall, however, this pressure gradient tends to vanish after $\sim 10d$ along Y -axis as we observed in Fig. 12 where we plotted the time-averaged axial confining pressure $\langle \sigma_{yy} \rangle$ as a function of the drum axial position y normalized by half length of the drum L for the sample of $\alpha = 5$. Figure 13.(a-b) shows the time-averaged force projected on Y -axis for the left-hand side of the drum f_{yl} in Fig. 13.(a) and for the right-hand side of the drum f_{yr} in Fig. 13.(b) (see left and right hand side of the drum zone in Fig. 8 left). Counter to the radial force f_r , the axial force (f_{yl} and f_{yr}) shows a clear tendency with the left hand being for his major part negative and the right hand being mainly positive with fluctuations that increase with the mean particle diameter on both sides.

6 Conclusions

In this paper, we used a 3D Discrete Element Method to study the effects of particle size ratio for a polydisperse granular material on the segregation process and its flow behavior in a rotating drum. The polydisperse samples composed of 50000 spherical particles were generated using PSD approaches with 4 dif-

ferent size ratios and were poured in a rotating drum composed of polyhedral elements and operating in the rolling regime.

The material flow was characterized at first by two regions in the drum radial axis where the flow is either governed by the gravity named active region or governed by the drum rotation within the contribution of the centrifugal force named passive region. By analyzing the evolution of the proportion of particles in four different zones during the flow, we evidenced two distinct migrations: 1) radial migration where large particles flow at the free surface and in contact with the drum polyhedra and, 2) axial migration where small particles migrate to the center of the drum. The two migration phenomena show an increase in the center (radially and axially) as the size ratio increases.

The segregation process was analyzed, and we were capable to explain the physical mechanisms that are at the origin of the process. Both axial and radial segregation have their origins in the fluctuation force and pressure gradient exerted on particles and the capability of small particles to fill pore spaces left behind by the large particles. While the pressure gradient for the radial segregation comes from the gravity and centrifugal force, the pressure gradient for the axial segregation is a direct consequence of the lateral wall effects. One can remove this axial pressure by using periodic boundary instead of the lateral wall as in some industrial processes with the goal is to homogeneously mix materials, but this can also be interesting if the goal is to separate particles based on their size.

Our results are based on a system of polydisperse granular materials up to a size ratio of 5; one can increase the size ratio using different types of PSD and analyze the spatial distribution of each size class at long-time simulation. From the same PSDs at higher size ratio, it also will be interesting to investigate the agglomeration processes when a part of the material is subjected to a cohesive force as the segregation phenomenon may affect the nucleation, coalescence, accretion, or erosion process that is important in mining, iron-ore making, and food industries for example.

Acknowledgments

This research is funded by Vietnam National Foundation for Science and Technology Development (NAFOSTED) under grant number 107.01-2020.24

References

1. D. Rapaport, *Physcal Review E* **65**, 061306 (2002)
2. G. Félix, N. Thomas, *Phys Rev E Stat Nonlin Soft Matter Phys* **70**, 051307 (2004)
3. D.C. Rapaport, *Phys Rev E Stat Nonlin Soft Matter Phys* **75**, 031301 (2007)
4. M. Arntz, W.K. den Otter, W.J. Briels, P. Bussmann, H. Beftink, R. Boom, *AIChE journal* **54**, 3133 (2008)
5. P. Chen, J.M. Ottino, R.M. Lueptow, *New Journal of Physics* **13**, 055021 (2011)
6. J. Third, D. Scott, C.R. Müller, *Physcal Review E* **84**, 041301 (2011)
7. R. Chand, M.A. Khaskheli, A. Qadir, B. Ge, Q. Shi, *Physica A: Statistical Mechanics and its Applications* **391**, 4590 (2012)
8. M. Arntz, H. Beftink, W.K. den Otter, W.J. Briels, R. Boom, *AIChE journal* **60**, 50 (2014)
9. C. Windows-Yule, B. Scheper, A. van der Horn, N. Hainsworth, J. Saunders, D. Parker, A. Thornton, *New journal of physics* **18**, 023013 (2016)
10. S. Yang, Y. Sun, Y. Zhao, J.W. Chew, *Physics of Fluids* **30**, 053301 (2018)
11. J.M.N.T. Gray, *AIP Conference Proceedings* **1227**, 343 (2010)
12. P. Frey, H. Lafaye de Micheaux, C. Bel, R. Maurin, K. Rorsman, T. Martin, C. Ducottet, *Advances in Water Resources* **136**, 103478 (2020)
13. D.J.W. Carson, *Drug Development and Industrial Pharmacy* **14**, 2749 (1988)
14. G. Seiden, P.J. Thomas, *Reviews of Modern Physics* **83**, 1323 (2011)
15. Y. Fan, K.V. Jacob, B. Freireich, R.M. Lueptow, *Powder Technology* **312**, 67 (2017)
16. J.M.N.T. Gray, *Annual Review of Fluid Mechanics* **50**, 407 (2018)
17. B. Marks, P. Rognon, I. Einav, *Journal of Fluid Mechanics* **690**, 499–511 (2012)
18. B. Marks, I. Einav, *Geophysical Research Letters* **42**, 274 (2015)
19. E. Alizadeh, O. Dubé, F. Bertrand, J. Chaouki, *AIChE Journal* **59**, 1894 (2013)
20. Z.S. Khan, W.A. Tokaruk, S.W. Morris, *Europhysics Letters (EPL)* **66**, 212 (2004)
21. H. Kuo, R. Hsu, Y. Hsiao, *Powder Technology* **153**, 196 (2005)
22. N. Jain, J.M. Ottino, R.M. Lueptow, *Granular Matter* **7**, 69 (2005)
23. T. Finger, A. Voigt, J. Stadler, H.G. Niessen, L. Naji, R. Stannarius, *Physcal Review E* **74**, 031312 (2006)
24. I. Zuriguel, J. Peixinho, T. Mullin, *Physcal Review E* **79**, 051303 (2009)
25. Z. Deng, Y. Fan, J. Theuerkauf, K.V. Jacob, P.B. Umbanhowar, R.M. Lueptow, *Powder Technology* **374**, 389 (2020)
26. L. Staron, *Physics of Fluids* **30**, 123303 (2018)
27. Z. Deng, P.B. Umbanhowar, J.M. Ottino, R.M. Lueptow, *AIChE Journal* **65**, 882 (2019)
28. G. Hill, S. Yeung, S.A. Koehler, *Europhysics Letters (EPL)* **72**, 137 (2005)
29. P.B. Umbanhowar, R.M. Lueptow, J.M. Ottino, *Annual Review of Chemical and Biomolecular Engineering* **10**, 129 (2019)
30. F. Guillard, Y. Forterre, O. Pouliquen, *Physics of Fluids* **26**, 043301 (2014)
31. F. Guillard, Y. Forterre, O. Pouliquen, *Journal of Fluid Mechanics* **807**, R1 (2016)
32. M.J. Woodhouse, A.R. Thornton, C.G. Johnson, B.P. Kokelaar, J.M.N.T. Gray, *Journal of Fluid Mechanics* **709**, 543–580 (2012)
33. C. Schlick, Y. Fan, P. Umbanhowar, J. Ottino, R. Lueptow, *Journal of Fluid Mechanics* **765**, 632 (2015), publisher Copyright: © 2015 Cambridge University Press.
34. Y. Fan, K. Hill, *New journal of physics* **13**, 095009 (2011)
35. Y. Fan, K. Hill, *Physcal Review Letter* **106**, 218301 (2011)
36. A. Samadani, A. Pradhan, A. Kudrolli, *Phys. Rev. E* **60**, 7203 (1999)
37. N. Engblom, H. Saxén, R. Zevenhoven, H. Nylander, G.G. Enstad, *Powder Technology* **215-216**, 104 (2012)
38. Y. Ding, R. Forster, J. Seville, D. Parker, *International Journal of Multiphase Flow* **28**, 635 (2002)
39. M. Newey, J. Ozik, S. Van der Meer, E. Ott, W. Losert, *EPL (Europhysics Letters)* **66**, 205 (2004)
40. C.P. Schlick, A.B. Isner, B.J. Freireich, Y. Fan, P.B. Umbanhowar, J.M. Ottino, R.M. Lueptow, *Journal of Fluid Mechanics* **797**, 95–109 (2016)

41. E. Alizadeh, F. Bertrand, J. Chaouki, *AIChE Journal* **60**, 60 (2014)
42. J. Mellmann, *Powder technology* **118**, 251 (2001)
43. J. Mellmann, E. Specht, X. Liu, *AIChE Journal* **50**, 2783 (2004)
44. R. Yang, A. Yu, L. McElroy, J. Bao, *Powder Technology* **188**, 170 (2008)
45. D. Li, G. Liu, H. Lu, Q. Zhang, Q. Wang, H. Yu, *Powder Technology* **291**, 86 (2016)
46. D. Li, L. Wang, Q. Wang, G. Liu, H. Lu, Q. Zhang, M. Hassan, *Applied Mathematical Modelling* **40**, 7708 (2016)
47. X.Y. Liu, E. Specht, J. Mellmann, *Chemical Engineering Science* **60**, 3629 (2005)
48. C. Voivret, F. Radjai, J.Y. Delenne, M.S. El Youssoufi, *Phys. Rev. E* **76**, 021301 (2007)
49. C. Voivret, F. Radjai, J.Y. Delenne, M.E. Youssoufi, *Physcal Review Letter* **102**, 178001 (2009)
50. T.T. Vo, N. Saeid, M. Patrick, D. Jean-Yves, I. Edouard, P. Roland, R. Farhang, *The European Physical Journal E* **42**, 127 (2019)
51. P. Mutabaruka, M. Taiebat, R.J.M. Pellenq, F. Radjai, *Phys. Rev. E* **100**, 042906 (2019)
52. P.A. Cundall, O.D.L. Strack, *Géotechnique* **29**, 47 (1979)
53. P.K. Haff, B.T. Werner, *Powder Technol.* **48**, 239 (1986)
54. H.J. Herrmann, S. Luding, *Continuum Mechanics and Thermodynamics* **10**, 189 (1998)
55. C. Thornton, *Powder Technology* **109**, 179 (1999)
56. F. Radjai, F. Dubois, *Discrete-element modeling of granular materials* (Wiley-Iste, 2011)
57. T.-T. Vo, *Erosion dynamics of wet particle agglomerates*, *Computational Particle Mechanics* **8** (2020) 601–612.
58. T.T. Vo, *Journal of Rheology* **64**, 1133 (2020)
59. M.P. Allen, D.J. Tildesley, *Computer Simulation of Liquids* (Oxford University Press, Oxford, 1987)
60. J. Duran, A. Reisinger, P. de Gennes, *Sands, Powders, and Grains: An Introduction to the Physics of Granular Materials*, Partially Ordered Systems (Springer New York, 1999), ISBN 9780387986562
61. V. Richefeu, F. Radjai, M.S.E. Youssoufi, *Eur. Phys. J. E* **21**, 359 (2007)
62. J. Schäfer, S. Dippel, D.E. Wolf, *J. Phys. I France* **6**, 5 (1996)
63. S. Dippel, G.G. Batrouni, D.E. Wolf, *Physcal Review E* **56**, 3645 (1997)
64. S. Luding, *Collisions and Contacts between two particles*, in *Physics of dry granular media - NATO ASI Series E350*, edited by H.J. Herrmann, J.P. Hovi, S. Luding (Kluwer Academic Publishers, Dordrecht, 1998), p. 285
65. T.T. Vo, P. Mutabaruka, S. Nezamabadi, J.Y. Delenne, F. Radjai, *Phys. Rev. E* **101**, 032906 (2020)
66. P.Y. Liu, R.Y. Yang, A.B. Yu, *Granular Matter* **15**, 427 (2013)
67. R. Aguado, S. Roudier, L. Delagado, eds., *Best available techniques (BAT) reference document for iron and steel production.*, Joint Research Centre of the European Commission (Luxembourg: Publications Office of the European Union, 2013)